Modeling Torso Imaging via
Time-Domain Diffuse Correlation Spectroscopy

by

Lorenzo C. Vigano

S.B., Electrical Engineering and Computer Science
Massachusetts Institute of Technology (2018)

Submitted to the Department of Electrical Engineering and Computer Science in partial
fulfilment of the requirements for the degree of

Master of Engineering in Electrical Engineering and Computer Science

at the

MASSACHUSETTS INSTITUTE OF TECHNOLOGY

June 2019

Author . . . .
Department of Electrical Engineering and Computer Science
May 24, 2019

Certified by . . . .
Megan H. Blackwell, PhD
Technical Staff, MIT Lincoln Laboratory
Thesis Supervisor

Certified by . . . .
Thomas Heldt, PhD
W.M. Keck Career Development Professor in Biomedical Engineering, MIT
Thesis Supervisor

Accepted by . . . .
Katrina LaCurts
Chair, Master of Engineering Thesis Committee

Modeling Torso Imaging via
Time-Domain Diffuse Correlation Spectroscopy

by

Lorenzo C. Vigano

Submitted to the Department of Electrical Engineering and Computer Science
on May 24, 2019, in partial fulfillment of the requirements for the degree of
Master of Engineering in Electrical Engineering and Computer Science

Abstract

Medical imaging is vital to the timely diagnosis of internal hemorrhaging and the prevention of fatalities. This thesis aims to contribute to this field by examining the efficacy of time-domain diffuse correlation spectroscopy (TD-DCS) as a means of imaging bleeding within the torso. TD-DCS is a new, powerful imaging technique with primary application of measuring blood flow in the brain.

Here we show both how this novel imaging technique can be expanded for use in other regions beyond the brain as well as how we hypothesized and modeled the technique's ability to detect internal bleeding consistent with the trauma-related injury of non-compressible torso hemorrhaging (NCTH). In the constructed models, blood thickness changes from four to six millimeters were detectable at the hepatic vein region within the liver. By using Monte Carlo models, trillions of photons were simulated to approximate results taken across a multi-second measurement. The results show promise for the technique and recommend the construction of a testbed for further testing.

Thesis Supervisor: Megan H. Blackwell, PhD
Title: Technical Staff, MIT Lincoln Laboratory

Faculty Supervisor: Thomas Heldt, PhD
Title: W.M. Keck Career Development Professor in Biomedical Engineering, MIT

Preface and Acknowledgements

This project introduced me to the complicated, useful world of optics, spectroscopy, and biomedical devices. With the never-ending support of my advisor, Megan Blackwell, I was able to tackle this project with excitement and vigor. I would also like to thank my friends Casey Evans and Julia Goupil for their constant stream of good ideas. Lastly, I want to thank my family. Your constant encouragement and love have been ever-present in my life. Every day, I feel blessed knowing the Viganos have my back.

While writing my thesis, I wanted to, as often as I could, make it accessible. The more people who immerse themselves in topics not immediately relevant to them, the more cross-disciplinary leaps that can be made, and often these are some of the most incredible steps forward. The investigation and creation of methods applicable for saving lives is a pursuit that, I feel, more people should devote their time to researching. Again, I am incredibly fortunate that I was given an opportunity to be able to contribute to this field.

Contents

List of Tables and Figures

1 Introduction and Background

Section 1 provides relevant information necessary to the understanding of the used spectroscopy and inference techniques, as well as a brief introduction into non-compressible torso hemorrhages.

1.1 Near-Infrared Spectroscopy

Near-infrared spectroscopy (NIRS) measures optical properties of a medium, such as absorption and scattering. These properties can be used for inferring flow, volume, and, in the case of blood, oxygenation. The original use-case of this technology, which this thesis aims to leverage for NCTH measurements, is for neuroimaging [1]. In that context, NIRS allows one to determine blood oxy- and deoxy-hemoglobin concentrations, which are important indicators of brain activity. The measurement process is relatively straightforward. A laser is directed at the tissue, and then measurements can be taken using models that consider the optical properties of the target tissue.

There are three widely used variants of NIRS: continuous wave (CW-NIRS), frequency domain (FD-NIRS), and time domain (TD-NIRS). In figure 1, shown below, there is a comparison between these three different methods. Leftmost is the continuous wave (CW) approach. This is the simplest of the three, and only requires a laser fired at the tissue. It then uses this light's attenuation to measure absorption. The frequency domain technique uses amplitude modulation. By measuring both attenuation and phase delay, FD-NIRS can infer information on scattering properties as well as absorption. Lastly, the time domain method quickly pulses the laser, then measures time-of-flight for these released photons. This allows data collection for absorption and scattering, as well as providing information for depth resolution. These pulses are incredibly short, a few picoseconds in duration, thus requiring precision and caution when measuring.
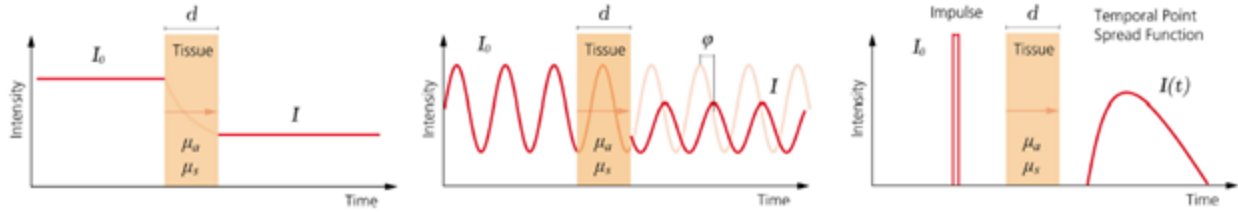
Figure 1: From left to right, CW-NIRS, FD-NIRS, and TD-NIRS. Used with permission

from Elsevier [2]

One important consideration is that FD-NIRS and TD-NIRS are fundamentally equivalent in the information they provide, as they are related through the Fourier transform. Despite having different experimental setups, they provide the same information. FD-NIRS, however, requires equipment that is much more complicated. Due to a need for modulated lasers and equipment capable of phasic measurements, FD-NIRS is both more technically challenging and expensive, thus making TD-NIRS the preferable technique.

1.2 Time Domain Diffuse Correlation Spectroscopy (TD-DCS)

This technique is analogous to TD-NIRS in that it too uses laser pulses to make its measurements, and thus the same techniques used by TD-NIRS for directly estimating optical properties of measured tissue can be applied. One such technique taken from TD-NIRS allows for measuring both the temporal point spread function (TPSF) and autocorrelation. Analysis of the TPSF allows for the use of photon diffusion theories that estimate optical properties of tissue directly. This is a huge advantage. Leveraging these established techniques allows for more development of TD-DCS in its applications. Keeping track of photon timing will be discussed more heavily in the later sections, but it is worth noting here that some forms of TD-DCS records both the photon arrival time with reference to the individual pulse and to the overall start time. Generally, less than one photon is detected on average per pulse. The shape of the pulse, constructed via the TPSF, is built by

aggregating hundreds of thousands of pulses together to create an accurate representation of the photon return timing distribution.

Another advantage of TD-DCS over TD-NIRS is TD-DCS's more direct measurement implementation. TD-NIRS laser pulses are extremely short, around four picoseconds in duration, and require incredible precision for their implementation. TD-DCS relies on a laser pulse with long coherence length. Pulses still need to be short to compute the TPSF measurement, but not too short that the pulse is shorter than the coherence of the light itself. The pulse width, therefore, that is acceptable for TD-DCS is 300 picoseconds (±200 ps) [3][4].

NIRS measures blood oxygenation and blood volume [5]. DCS measures blood flow, in which continuous wave methods can provide relative blood flow measurements and pulsed methods can return absolute values through BFi, which is often given in units cm^2/s. TD-DCS combines these two techniques to measure all three. This is important because with all three parameters, much more information can be pieced together. For example, with all three parameters, an estimate of cerebral metabolic rate of oxygen can be approximated. This measurement gives insight into brain activity, is normally hard to measure, especially continuously, and often requires invasive methods; TD-DCS can make this measurement non-invasively [4].

An important aspect of the optical techniques is the range of both temporal and spatial sensitivity. The ultimate goal of TD-DCS is as a technique for imaging the human body, whether the head and brain or the torso. Devices within the field of human imaging range in temporal and spatial capabilities depending on their usages. For example, functional magnetic resonance imaging (fMRI) has a high spatial resolution, meaning it can image within the range of about 4-millimeter accuracy. fMRI is a common way to image the brain, but with its slow temporal resolution, offers limited ability to measure blood flow [6]. By comparison, TD-DCS has a higher temporal resolution. This means that TD-DCS is more

adept at measuring changes with respect to time; however, it has poorer spatial resolution when compared to MRI. Another important consideration is size. A fMRI machine is large, as well as expensive, and cannot be moved. TD-DCS technology lends itself to being much more portable.

1.3 Photon Detector Gating

One of the essential components of a TD-DCS experimental set-up, in addition to the laser, is the photon detector. Single-photon avalanche diodes (SPADs) are highly effective photon detectors that need only one incident photon to be triggered. However, one inherent restriction with photon detectors is their dead time. After a photon is detected, a chain reaction of electrical impulses is stimulated followed by a window of time in which photons cannot be detected. If a new photon were to hit the detector during this time, it would go unnoticed. This dead time is usually around one microsecond for a typical InGaAs detector, which could potentially be a problem on the TD-DCS timescale. One approach, which does help with shortening dead time, is construction of a macropixel. A macropixel approach spreads out the optical signal across multiple pixels of a detector; therefore, even if one pixel detects a photon, the others still are armed and ready to detect photons [7].

As described earlier, the TPSF, which is equivalent to the probability distribution function of the return photon times with respect to the laser pulse, is constructed by compiling the returns from multiple laser pulses. By gating the detector, or using a technique in which the detector is strategically armed during specific times, the early-arriving photons that have only traveled through the more superficial layers of scalp and skull can be ignored. Without gating, it would be highly improbable to detect any photons except the photons that were first to return and thus traveled the least distance into the target tissue. Any photons that traveled farther into the tissue and then returned to the detector would not be counted

because the detector would still be resetting from its detection of the earlier photon. Gating sets a window to arm the SPAD so that these early photons will not trigger a detector and so the SPAD can be ready to detect a later arriving photon. Another powerful application of gating is in its ability to be used to select for specific regions in the tissue. Given familiarity of the target tissue and its layers, gating the SPAD for a precise window of time can select for photons that, with high probability, are returning from a specific layer.

1.4 Tissue Optical Properties

With respect to the modeling performed for this thesis, and the larger world of organic tissue optics, there are four very important wavelength dependent considerations: scattering coefficient μ_s, absorption coefficient μ_a, index of refraction n, and the average cosine of scatter g. With these data on tissue types, complex Monte Carlo simulations, amongst many other more tangible models, can be constructed and investigated.

When a photon transitions into a new medium, the first important consideration is the index of refraction, which is the integral component of Snell's law and determines how much a photon will be deflected upon entering a medium with a different index of refraction than that of its current medium. While initially one would attempt to fire the photons at an angle zero degrees from the normal of the tissue, and thus the index of refraction would be unimportant, after one or more scattering events, a photon's path will no longer be perfectly perpendicular to the medium interfaces through which it passes.

The absorption coefficient correlates directly with the amount of data received, and thus is nearly as important as the scattering coefficient. In a theoretical world with no absorption, photons would continue to scatter indefinitely. Detection would then rely only on whether or not the eventual path intercepted with photon detector, for example a SPAD, and was detected. Unfortunately, organic tissues have absorptive components. Intuitively, the

absorption coefficient can be thought of as a variable representing how likely a photon is to be absorbed when moving through a medium. More technically, $1/\mu_a$ is the distance over which light intensity is reduced by 37% (e^{-1}) from its original intensity. This relationship comes from the Beer-Lambert Law $I = I_0 e^{-\mu_a z}$, in which z is thickness, generally in cm.
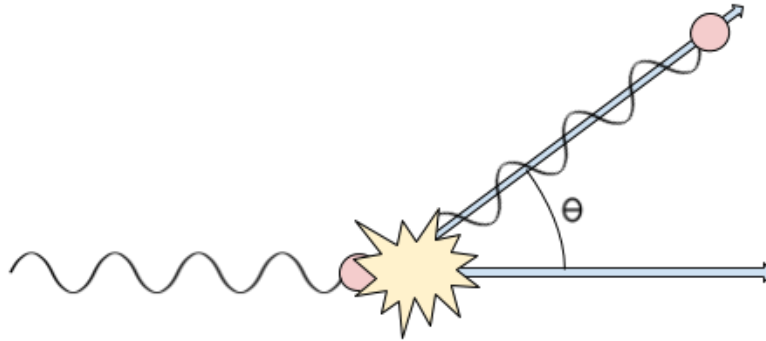
Figure 2: A photon scattering event

Given that a photon has scattered, θ represents the scattering angle and thus $g = cos(\theta)$. For example, if, on average, the tissue perfectly rebounds the photons, g would be -1 and if the scattering event has no impact on the trajectory, g would be 1.

The most important factor for this project, and this imaging modality, is the scattering coefficient. In mammalian tissues, often scattering is the dominant factor affecting the propagation of photons [8]. Similar to how intensity decreases as a function of μ_a, intensity also reduces with μ_s following the Beer-Lambert Law. While they both affect light in the same way, tissue is far more scattering than absorptive at the wavelengths used for near-infrared imaging. For example, in the experiments shown in Section 2, μ_s is around 1000 times larger, on average, than μ_a.

1.5 Blood Flow Calculations and Autocorrelations

One important mathematical analysis technique used by TD-DCS methods to determine blood flow is an autocorrelation. An autocorrelation is the convolution of a signal with a delayed copy of itself as a function of the delay [9]. By analyzing the autocorrelation, patterns and periodic events can be found. This technique is used in TD-DCS analysis to determine the blood flow index (BFi). The rate of decay of the autocorrelation curves is proportional to the flow rate; faster decay indicates higher blood flow.

Originally developed by the inventors of TD-DCS [10], the calculation of blood flow is a multistep process relating the autocorrelation of the propagation of the electric field inside tissues, shown in Equation 1, and the autocorrelation of the measured photon intensity.

$$G_1(r, \tau) = \langle E(r,t), E^*(r, t+\tau) \rangle \tag{1}$$

Because directly measuring the electric field is extremely difficult, the value for G_1 can be modeled by using the photon correlation diffusion equation (Equation 2), which is another important contribution of Boas and co-workers [11]. Here, μ_s and μ_a refer to the scattering and absorption coefficients respectively, k_0 is the light diffusion constant, v is the speed of light in the medium, and $S\delta^3(r - r_s)$ represents the point source located at r_s.

$$\nabla \left[\frac{v}{3\mu_s'} \nabla G_1(r, \tau) \right] - G_1(r, \tau) \left[\frac{1}{3} v\mu_s' k_0^2 \alpha \langle \Delta r^2(\tau) + v\mu_a' \rangle \right] = -vS\delta^3(r - r_s) \tag{2}$$

$$g(r, \tau) = \frac{G(r, \tau)}{G(r, 0)} \tag{3}$$

$$g_2(r, \tau) = 1 + \beta |g_1(r, \tau)|^2 \tag{4}$$

The BFi can be calculated using the relationship between the normalized intensity autocorrelation, g_2, and the normalized electric field autocorrelation, g_1, (Equation 4), combined with the relationship between $\Delta r^2(\tau)$, the mean-square displacement, and the effective Brownian motion coefficient. Analysis of TD-DCS measurements provides enough

information to calculate the intensity autocorrelation through the returning photons, and thus determine blood flow.

While the biophysics and derivations of these equations are outside the scope of this thesis, it is necessary to understand the importance of these equations and autocorrelations because they allow for the calculations that determine blood flow.

1.6 Non-compressible Torso Hemorrhage (NCTH)

A leading cause of potentially preventable military trauma deaths is the result of non-compressible torso hemorrhage (NCTH) [12]. Specifically, NCTH is a trauma-related injury resulting in internal blood loss, often affecting larger arteries and veins, such as the Inferior Vena Cava [13]. Because these injuries are within the torso, they are not easily stanched and often require medical procedures within hospitals. NCTH is also a concern for civilians. During a 10-year study in the UK, patients who were identified to have NCTH had a mortality rate of 85.5% when no surgical intervention was available. Patients who were admitted to the hospital, however, had a mortality rate of 58.1% when surgical intervention was available [14]. This injury is lethal, especially outside of the hospital. It requires surgical intervention, and this requires the precise knowledge regarding the location of the injury within the torso. Within a hospital, diagnosis via computed tomography CT is effective. In the field, however, adequate imaging, such as the aforementioned fMRI and CT devices, are far too large and expensive to be practical.

This is where a TD-DCS device could be useful. Due to its necessary measurement equipment being small, TD-DCS technology could conceivably be packaged into a portable unit that could be used at the bedside or in the field. While this miniaturization is not a goal of this thesis, it is an accomplishable task, and thus considering its application for NCTH identification is reasonable. The more important considerations will be the depth and

resolution achievable via TD-DCS within the torso. Modeling and measurements will play a large part in these determinations.

2 Completed Work

2.1 Modeling

Before diving headfirst into prototyping and building, it is critical to appropriately gauge the probability of success, especially when high-precision timing is required. When it comes to equipment, it generally follows that the smaller the time scale resolution, the more expensive the equipment. If a project were deemed to have a low probability of success through modeling, then money would have been saved by not needing to purchase equipment and then discover something does not work. Another important reason modeling is an important first step in a research project is the restrictions upon testing with human subjects.

One important goal of this thesis was to create a modular set of programs, functions, and an experimental layout that another researcher, interested either in the torso or in another section of the body would be able to use as a starting point. In the section below, each step of the process will reference an individual file that is included in section 4, Code Library. Ideally, someone could take, adapt, and use these files to model other sections of the body, and find their own results.

### 2.1.1 Existing Modeling Technology

Given that modeling is such an important step in scientific research, there exist many frameworks for constructing models and tools to help facilitate the process. Within the field of Monte Carlo simulations, and more specifically photon simulations, there are fewer tools. Of the few publicly available tools for this type of simulation and research, two, both created

by a group at Northeastern University in the Department of Bioengineering, were suitable for this thesis: Monte Carlo eXtreme (MCX) and Mesh-based Monte Carlo (MMC).

MCX is described as 'a photon simulator for modeling light transport in 3D turbid media' [15]. MMC provides a similar set-up for experimentation with two main differences. MMC can represent a more complex domain using a volumetric mesh. This would allow for a user to model objects that have curved boundaries, such as an entire organ. This capability, while important for some users, is not necessary for modeling the torso in the granularity considered. Given the size of the model, which will be further discussed in the following section, the transitions between layers can be approximated as flat, and the small curvatures that could be modeled with MMC would not significantly affect the results. The second, and critical, difference is MMC's lack of GPU support. The simulations performed in this thesis took advantage of the MIT Lincoln Laboratory Supercomputing Center, which provided access to several different types of GPUs that used the Supercomputing Center's grid [16]. The ability to run billions of photon simulations simultaneously across multiple GPUs allowed experiments to be run relatively quickly and with high enough numbers of photons to trust the output results. The more photons simulated, the more the aggregate results of the random events can be thought to represent the true behavior of the modeled experiments. Thus, this thesis uses the MCX framework software for running the photon simulations.

2.1.2 Model Overview

Shown to the right is a pictorial representation of the constructed model. The right-most model is identical to the left most, with the addition of a blood layer. From top to bottom, the different blocks represent the layers traversed by a
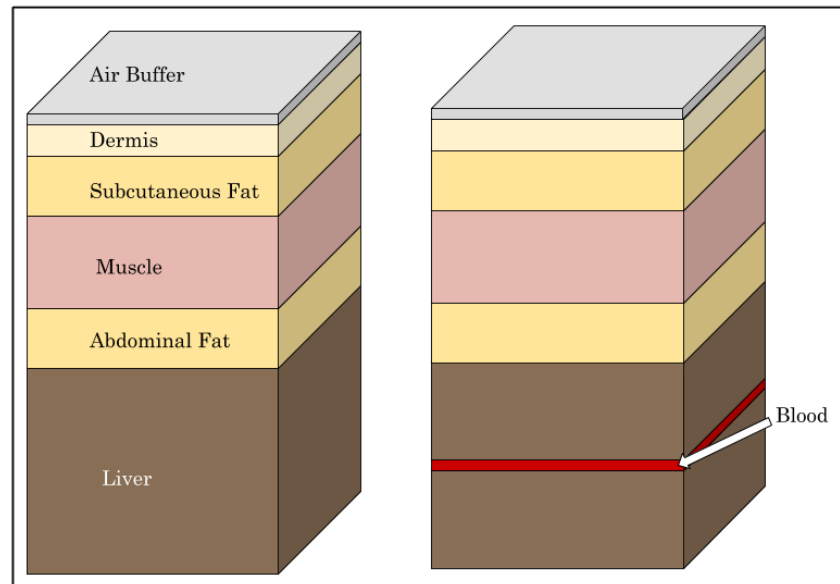
Figure 3: Model overview

photon from the surface to the back of the liver. In order, the layers are air, dermis, subcutaneous fat, muscle, abdominal fat, and finally liver. This section is centered just below the sternum, level with the T-11 vertebrae. As mentioned earlier, one common NCTH location occurs in the inferior vena cava and hepatic veins. This line of sight, from the dermis to the back of the liver includes both the hepatic veins and inferior vena cava. While other veins such as the superior mesenteric vein are also of interest for NCTH, this model was a good place to start and investigate proof of concept and feasibility [17].

The following sections will first explain the general process for creating and running a specific simulation and model configuration, and then discuss the differing simulations and what each one hopes to answer, followed by results and analysis.

2.1.3 Data Flow
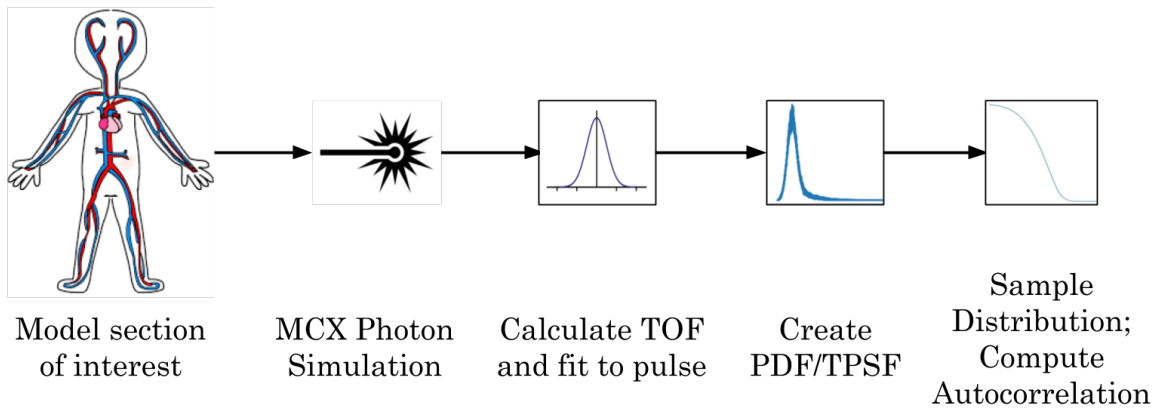
Figure 4: Data flow of an experiment

The flow of data for one sample experiment starts with creating the model file. *CreateMCXConfig.m* formats data into a JSON file to be imported by the MCX program. For each layer added, both layer thickness and respective optical properties (μ_a, μ_s, g, n) are added, as well as the number of photons to be simulated and over what time period.

After constructing the model files, they are uploaded into MCX, which runs each photon's simulation independently on a GPU. The resulting photon path is stored in a .mch file. Important note: the only photons stored in the .mch file are those that returned, and thus seen by a detector. Each 25 mW 300 ps pulse generates roughly 0.5 GB of data. In order to determine an accurate average, 1000 pulses are simulated, resulting in nearly half a terabyte of data for just one model configuration. It is essential to extract the relevant information from the photon paths and create a way to analyze the data in a reasonable amount of time.

For each simulation, it is important to know both the penetration depth achieved and then the more nuanced timing characteristics. Before converting the photon paths to time-of-flight times, every path is checked to find the deepest layer of penetration for that photon and a composite frequency table is generated. Due to the large and dense nature of the liver,

for this model, the liver was divided into four regions: the superficial portion, the area surrounding the hepatic vein, another deeper posterior region, and finally the section of liver bordering the inferior vena cava. After determining if a specific model configuration had the necessary penetration, timing calculations began.

Creating the TPSF is a multistep process beginning with converting each photon path to a time stored in picoseconds. The path of the photon is constructed as distance traveled within each layer. The total time of flight is calculated by summing the times the photon spends in each individual region. The formula for calculating the time spent in one region is shown below, where distance is given in grid units, thus millimeters, n_{region} is the index of refraction for the given region, and c is the speed of light.

$$Time_{region} = \frac{distance_{region} * n_{region}}{1000 * c} \qquad (5)$$

Once the total time is calculated, it is stored in an array along with all other calculated times. The GPU computes each photon simulation in parallel. Therefore, two extra steps of post-processing are required to construct a sample pulse: randomize the order of the photons and artificially fit them to a curve. The rational for randomizing the photon array comes from the uncertainties of the inner workings of MCX. Due to the possibility of an internal bias, such as sorting by length of path, it is necessary to randomize the data before fitting to a curve.

Fitting the photons to an input pulse curve is very important for capturing real world equipment behavior. Any laser will have a ramp up and ramp down time, and in the case of TD-DCS measurements, there is a balance between needing a short pulse-width and having to maintain the coherence length of the laser. Short pulse-width makes analysis of the return pattern simpler, however, maintaining the coherence is necessary so that the non-coherence

seen at later times delays in the autocorrelation analysis is due to tissue properties and not laser incoherence.

Fitting the photons to the desired curve requires adding a delay to the photons stored in the array. The cumulative distribution function (CDF) that describes the shape of the laser pulse is used to create a histogram for curve fitting. For this project, a Gaussian pulse with mean 150 ps and a standard deviation of 50 ps is used as a model laser pulse. Starting at time zero, and then incrementing forward one picosecond at a time, the CDF determines how many photons will be 'released.' The final photon time will be the sum of its traversal time and the time it was delayed, which models the real-world equivalent of leaving the laser later. This new array now contains the final, real time-of-flights for each photon, which can be used for analysis and constructing an autocorrelation. These values are stored in a .txt file, about 0.2 GB in size. The above calculations and data manipulations are made by *mch_txt.m*.

The data, in its current form, while smaller is still far too large to compute the autocorrelation in a reasonable time. Even with fast computers, computing the autocorrelation on data of this size would take hours. If a patient has a potentially fatal injury, this is far too long to wait for results. This provides motivation for decreasing the size of the data and computation time, and though the format of the data from this modeling would be different from the format of data on a potential device, this scenario provides justification for desiring smaller data sizes and faster result acquisition time. On average computation of 10 seconds worth of data requires about two seconds of final processing. This benchmark is sufficiently fast for a situation where time is vitally important.

At this stage in the modeling, the information is also currently stored with more detail and fidelity than would be achievable by real-world measurements. Therefore, the data is turned into a histogram with 0.5e-13 second width bins. Normalizing and calculating weights for each bin gives a PDF, equivalently a TPSF, which can then be sampled infinitely many

times. The 1000 generated pulses are all combined into this histogram to make an accurate PDF, which is easy to sample and creates photon times that represent the return pattern of the underlying model. This step is done in *create_pdf.py*. From here, arbitrarily long signals can be created. Sampling from the PDF can be repeated in various ways in order to create whatever type of pulse desired. *sample.py* shows an example of loading in the weights stored in the JSON file and sampling at one photon per pulse.

After generating times, these values are stored in an array to then be passed into *autocorrelation.py* where the autocorrelation computation begins. The autocorrelation of the signal will be essential in both qualitative comparative analysis between different modeled experiments, as well as flow calculation in real-world measurements.

2.1.4 Laser and Detector Properties

In an ideal scenario, the more photons fired into the tissue, the better, as this would increase the number of photons that potentially penetrate the relevant tissue layer and then return. Unfortunately, however, the intended target tissue is living human tissue, and without proper precaution and power limiting, serious harm could be done. The American National Standards Institute has guidelines for using lasers on humans, both for optical and dermal energy deposition [18]. Following these standards, lasers can be appropriately designed for use on humans. ANSI Z136.1 has very specific limits for nearly every combination of laser wavelength, pulse width, and periodicity. To find the power limit for a specific experiment, ANSI equations need wavelength, aperture, distance from tissue, and, if it is a pulsed laser, which TD-DCS uses, the pulse characteristics are needed. Following their equations and guidelines, all experiments using a 920 nm, and below, wavelength laser are limited to 25 mW of power, or 40,140,000 photons across the 300 ps pulse. While the 1064 nm

and 1120 nm wavelengths have an ANSI limit of 100 mW, the same output power of 25 mW was used across all experiments for continuity.

In addition to limiting the laser power to 25 mW, the laser was also modeled to be a safe 2 mm away from the first tissue layer and was chosen to have a Gaussian cone [18], so that the light was not focused a single point, but rather dispersed across a small circle with one-millimeter diameter on the dermis. Spreading the photons across more tissue was another strong recommendation of ANSI. However, having a focused beam is important for limiting horizontal dispersion.

The only decision for modeling the detectors was in their placement. Generally, the farther the detectors from the laser, the deeper resolution obtainable [19]. If, for example, a detector records a photon arrival after a period of time and this detector is far from the laser source, this photon is more likely to have taken longer to arrive at the detector and probably traveled in the deeper layers before surfacing. If a detector that was closer to the laser source marks a photon arrival at the same time, it was more likely that this photon was one that only traveled shallow into the tissue and thus took a shorter time to return. Therefore, to maximize capture of photons that likely penetrated farther, four detectors were placed each one millimeter away from the laser, one in each of the four cardinal directions.

2.1.5 Tissue Layer Properties

The following tables display the values for tissue thickness and optical properties. For each experiment, unless stated otherwise, these are the values used in simulation. Values for optical properties were chosen with preference given to studies that took measurements *in vivo*, and were more recent. If values could not be found at a specific wavelength, then the value was determined via trends and has been marked with an *.

Table 1: Tissue Layer Thickness

Tissue Layer	Thickness (mm)
Dermis	2 [20]
Subcutaneous Fat	11 [21]
Muscle	17 [22][23]
Abdominal Fat	16 [24]
Liver	35 [25]
Blood	5 [26]
Liver	37 [25]

Table 2: Optical Properties (μ_a, μ_s, g, n)

Tissue Layer	Wavelength (nm)	μ_a (mm^{-1})	μ_s (mm^{-1})	g	n
Dermis	765	0.013 [27]	17* [28]	0.8 [27]	1.42 [29]
	820	0.011 [27]	14* [28]	0.8 [27]	1.42 [29]
	920	0.008 [27]	11.3* [28]	0.86* [28]	1.42* [29]
	1064	0.005 [27]	8* [28]	0.8 [27]	1.38 [29]
	1120	0.008 [27]	8.5* [28]	0.8 [27]	1.37 [29]
Subcutaneous Fat	765	0.11 [30]	12.7 [30]	0.91 [31]	1.44 [31]
	820	0.107 [30]	12.9 [30]	0.91 [31]	1.44 [31]
	920	0.107 [30]	11 [30]	0.91 [31]	1.44 [31]
	1064	0.106* [30]	10* [30]	0.91 [31]	1.44 [31]
	1120	0.105* [30]	9.4* [30]	0.91* [31]	1.44* [31]
Muscle	765	0.04 [30]	19.3 [30]	0.96 [31]	1.37 [31]
	820	0.03 [30]	17.3 [30]	0.96 [31]	1.37 [31]
	920	0.04* [30]	15.3* [30]	0.96 [31]	1.37 [31]
	1064	0.1* [30]	13.2* [30]	0.96 [31]	1.37 [31]
	1120	0.15* [30]	12.5* [30]	0.96 [31]	1.37 [31]
Abdominal Fat	765	0.002 [32]	16.6 [32]	0.91 [31]	1.37 [32]
	820	0.005* [33]	11.1* [33]	0.91 [31]	1.37 [32]
	920	0.18 [30]	10* [33]	0.91 [31]	1.37 [32]
	1064	0.3 [31]	3.7 [31]	0.91 [31]	1.46 [31]
	1120	0.22 [33]	4.4 [33]	0.91 [31]	1.37 [32]
Liver	765	0.175* [34]	32.5* [34]	0.75* [34]	1.38 [31]
	820	0.17 [34]	33.1 [34]	0.83 [34]	1.38 [31]
	920	0.1 [34]	34.3 [34]	0.87* [34]	1.38 [31]
	1064	0.07 [34]	35.6 [34]	0.95 [34]	1.38 [31]
	1120	0.045 [34]	36.3 [34]	0.96 [34]	1.38 [31]
Blood	765	0.53 [35]	72.5 [35]	0.991 [35]	1.37 [36]
	820	0.66 [35]	68 [35]	0.99 [35]	1.37 [36]
	920	0.89 [35]	65 [35]	0.992 [35]	1.37 [36]
	1064	0.56 [35]	64.5 [35]	0.992 [35]	1.363 [36]
	1120	0.47 [35]	63.9 [35]	0.993 [35]	1.36 [36]

2.1.6 Assumptions

For the liver model, a few assumptions and simplifications were made during simulations to both reduce complexity and lower the amount of data stored. One assumption that would surely not hold in an actual measurement would be the ideal nature of the laser, detector, and other facilitating equipment. For example, some of the most efficient InGaAs/InP SPADs have a detection efficiency of 40%, while the faster silicon detectors have a detection efficiency of 5%. The modeled detectors, using MCX software, record every photon that they encountered. While discarding 95% of the photons randomly could be a method to more accurately simulate total photon acquisition, certain modes of loss, such as after-pulsing and dark count, are not entirely random [37]. Modeling photon detectors is an incredibly complicated field of research and thus outside the scope of this thesis.

Within this thesis's simulations, unless it was meant to be ignored, every photon was tracked and counted. Not only is this nearly impossible in the real world, it is slightly unnecessary. To make TD-DCS measurements, only the return photon timestamps are needed. Simulation, however, provides not only this, but also the actual path taken by each photon. While this could give useful insight into how photons are behaving within each tissue layer, it is useless for TD-DCS measurements, and thus, as explained in section 2.1.3, was discarded.

Although the model was simplified for the purposes of this thesis, these simplifications do not affect the signal integrity. This thesis aims to demonstrate that the technology described could be used for this type of use-case and that it would have the necessary tissue penetration and feedback signal to make TD-DCS measurements. Laser and detector non-idealities would potentially influence the number of photons both fired and detected, but they would not affect the trajectories of photons. The mostly likely consequence would be a

requirement of longer acquisition time before capturing enough data to make a measurement or diagnosis.

2.1.7 Process and Experiments

The ultimate goal of the thesis is to determine the feasibility of TD-DCS to be used to model the torso and extrapolate information relevant to a use-case such as NCTH identification. Across the 20 experiments conducted for this thesis, three attributes were varied: light wavelength, blood layer thickness, including a thickness of 0, and optical properties of a specific tissue type.

In order to exhaust the NIRS range of wavelengths, multiple experiments were conducted at varying wavelengths. 765 nm, which is a popular wavelength used in NIRS technologies, 1064 nm, which has recently shown promise with respect to penetration and TD-DCS measurements [38], and several other wavelengths were all tested to capture a wide range of the near infrared spectrum. Varying wavelength affects the optical properties of each tissue layer, sometimes dramatically. For example, blood's μ_s decreases 11.86% when changed from 765 nm to 1120 nm.

One crucial component of this thesis, which will be heavily discussed in section 2.2, is blood detection. Thus, five experiments were conducted with the default optical properties, one for each wavelength, and five identical experiments were run, but with the addition of a 5 mm layer of blood inserted after the hepatic liver region. These tests will provide a comparison to determine if identification of a blood layer at specific wavelengths is possible. The results of these experiments are shown in Table 3 and Table 4.

After these experiments were made, simply looking at photon depth penetration was enough to determine which wavelengths were viable: 1064 nm and 1120 nm. At these wavelengths, eight more experiments were conducted in which the blood layer thickness was

varied. These tests help to determine the fidelity of the system, as well as whether the thickness of the blood plays a large role in the return signal. Results from these tests are shown in Table 5 and Table 6.

Finally, in an effort to confirm that these experiments are not solely reliant on the optical property values used, a 'worst-case scenario' test was run in which μ_s and μ_a of a tissue layer were each increased by 5%. The liver was selected, as it was both the thickest of all layers and one of the most absorptive and scattering of all the tissue types. If this perturbation were enough to skew the photon depth penetration, then the results of all other tests would be considered precarious. Results are shown in Table 7.

2.1.8 Results

In Tables 3-7, for each tissue layer, the number of photons represents the photons that reached their maximum tissue penetration in that layer. For example, the photons that reached the layer of abdominal fat did not reach the liver, but did pass through the dermis, subcutaneous fat, and muscle layers. Therefore, the total number of photons that reached a layer is the sum of the current cell and all below it in the same column. For example, in Table 3, the number of photons that reached the Liver Hepatic region for 1064 nm is 119.

Table 3: Photon Penetration without Blood Layer (25 mW)

Tissue Layer	765 nm	820 nm	920 nm	1064 nm	1120 nm
Dermis	1.860e10	1.689e10	1.490e10	1.165e10	1.222e10
Subcutaneous Fat	4.750e8	6.096e8	6.832e8	8.973e8	8.053e8
Muscle	7.707e6	8.090e6	9.640e6	1.140e7	1.117e7
Abdominal Fat	5.552e5	5.295e5	6.379e5	4.459e5	5.244e5
Liver	4.063e4	5.197e4	6.286e4	8.070e4	7.603e4
Liver Hepatic	0	0	2	77	107
Liver	0	0	0	42	66
Liver IVC	0	0	0	0	0

Table 4: Photon Penetration with Blood Layer (5 mm)

Tissue Layer	765 nm	820 nm	920 nm	1064 nm	1120 nm
Dermis	1.8597e10	1.6886e10	1.490e10	1.165e10	1.222e10
Subcutaneous Fat	4.750e8	6.095e8	6.833e8	8.973e8	8.053e8
Muscle	7.706e6	8.090e6	9.645e6	1.140e7	1.117e7
Abdominal Fat	5.565e5	5.304e5	636112	4.455e5	5.223e5
Liver	4.066e4	5.191e4	6.296e4	8.042e4	7.633e4
Liver Hepatic	0	0	1	73	119
Blood	0	0	0	14	15
Liver	0	0	0	19	39
Liver IVC	0	0	0	0	0

Table 5: Changing Blood Layer Thickness

Tissue Layer	1064nm 2mm	1064nm 4mm	1064nm 6mm	1064nm 8mm
Dermis	1.165e10	1.165e10	1.165e10	1.165e10
Subcutaneous Fat	8.9731e8	8.973e8	8.974e8	8.974e8
Muscle	1.140e7	1.140e7	1.140e7	1.140e7
Abdominal Fat	4.461e5	4.456e5	4.470e5	4.459e5
Liver	8.046e4	8.047e4	8.035e4	8.067e4
Liver Hepatic	86	78	67	79
Blood	8	13	18	20
Liver	25	16	14	9
Liver IVC	0	0	0	0

Table 6: Changing Blood Layer Thickness cont.

Tissue Layer	1120nm 2mm	1120nm 4mm	1120nm 6mm	1120nm 8mm
Dermis	1.2219e10	1.2219e10	1.2219e10	1.2219e10
Subcutaneous Fat	8.053e8	8.053e8	8.053e8	805247750
Muscle	1.116e7	1.116e7	1.117e7	1.117e7
Abdominal Fat	5.236e5	5.230e5	5.231e5	5.237e5
Liver	7.676e4	7.601e4	7.622e4	7.618e4
Liver Hepatic	111	93	105	112
Blood	5	8	14	20
Liver	49	30	26	16
Liver IVC	0	0	0	0

Table 7: 5% Optical Property Change in Liver

Tissue Layer	1064nm 5mm	1120nm 5mm
Dermis	1.165e10	1.222e10
Subcutaneous Fat	8.973e8	8.053e8
Muscle	1.140e7	1.117e7
Abdominal Fat	4.459e5	5.221e5
Liver	8.128e4	7.739e4
Liver Hepatic	91	108
Blood	5	16
Liver	17	23
Liver IVC	0	0

2.2 Analysis

With the ultimate goal being the determination of feasibility of TD-DCS as a measurement technique to identify internal bleeding within the torso, three factors were necessary to test: photon penetration, timing and measurability, and autocorrelation differences. By simply looking at photon penetration, depth penetration can be seen and baseline feasibility for use as NCTH identification test can be considered. For example, if photons cannot even reach the hepatic layer in the liver, then that configuration could be ignored as a viable option. If a configuration does have photons that reach the required layers, then TD-DCS techniques, such as gating and autocorrelation analysis, can be used. Another important consideration is measurability. While it may be possible to differentiate between models with blood and without blood in simulation, the differences need to be large enough that they can be measured by real-world equipment within a reasonable amount of time.

2.2.1 Photon Depth Penetration

Photon depth penetration is one of the most essential factors in determining the viability of the system. Without photons reaching a layer, it would be impossible for analysis methods to determine anything about that layer. Tables 3-7 contain the information for depth penetration.

In terms of depth penetration only, a NCTH measurement, with the goal of measuring flow in the hepatic veins within the liver, is plausible for a measurement time of 10 seconds only at wavelengths of 1064 nm and 1120 nm. No photons at wavelengths 765 nm, 820 nm, nor 920 nm reached the region of interest, and thus were eliminated from consideration and further analysis. A longer acquisition time would enable more averaging to be performed and may make other wavelengths viable. This was beyond the scope of this thesis.

The results of an important viability test are shown in Table 7. One important check on any set of results is the determination of how reliant the results are on the chosen parameters, in this case the optical properties. If a slight deviation from the parameters were to render seemingly viable wavelengths inviable, then there would potentially be a reason to doubt the entire model. Fortunately, the results of Table 7 show that for both 1064 nm and 1120 nm wavelengths, given an altered set of optical properties, photons were still able to penetrate to the region of interest. The 5% increases in both μ_s and μ_a within the liver were substantial changes, and enough to be considered an adequate perturbation in the input properties. Of all the tissue layers within the model on the path to the blood layer, the liver layer was the thickest, most reflective, and the most absorptive. Adjusting this layer, while still not deviating too far from the properties found in current literature, constitutes an appropriate test and implies that the results for the unchanged 1064 nm and 1120 nm experiments can be viewed as reliable.

2.2.2 Timing and Measurability

The motivation behind modeling is to determine whether a method would be viable, and whether it is worthwhile to move forward with prototyping and then further construction of the idea. This determination of viability is two-fold. The technique must perform adequately within the modeling, where adequate performance is determined by the use-case,

and the technique needs to be able to be replicated in the real world. That is to say, something could work in modeling, but that does not mean that the physical world has the capability of implementing the method, and this, too, must be considered. The focus of the analysis thus far has been on whether TD-DCS is performing well in the model, but this section will examine its viability outside of the model by looking at timing and measurability.

The essential component to TD-DCS is the fidelity and precision of the photon firing and photon detection timing. Some of the results above are compelling and show that it is possible that TD-DCS could work in the real world. However, there is still an important limitation that could prevent this: the availability of measurement equipment necessary for obtaining differentiable results.

Shown below is a table comparing the average time of flight for photons at their respective wavelength, both with and without blood layers. This data was taken by assuming one photon returns per laser pulse for 10 seconds worth of data with a laser pulsing at 80 MHz. This results in 800,000,000 photons.

Table 8: Average Time of Flight

Wavelength	With Blood	Without Blood
765 nm	1.763e-10	1.765e-10
820 nm	1.778e-10	1.778e-10
920 nm	1.785e-10	1.785e-10
1064 nm	1.806e-10	1.805e-10
1120 nm	1.794e-10	1.794e-10

As seen above, the difference in timing is minuscule, and thus there are no discernable patterns. Even for both 1064 nm and 1120 nm, there is not a consistent difference between the average time with blood and without blood. Because the blood layer is highly reflective, it is expected that the average time for a photon from the model without blood would be longer, as it would be able to penetrate deeper into the liver, having not been reflected by the blood. Unfortunately, due to how small a number of photons actually reach the back of the

model, the differences in the average time are skewed mostly by random chance and differences in previous identical regions. For example, looking at Table 3 and Table 4, by no cause other than chance, a larger number of photons were reflected in the subcutaneous fat layer in the model without blood than in the model with blood.

Not only is there no discernable pattern, but the measurability of the above data would be very difficult in the real world; any differences that do exist are sometimes in femtosecond range. Only with extraordinarily advanced measurement equipment can these changes be noticed, requiring both incredible precision of both the photon detector and the accompanying timing equipment. This does not lend itself to being cheap nor portable. By incorporating gating, however, there is a potentially better outlook.

The same analysis can be run while also incorporating a gate, thus ideally eliminating these biases. The gate timing for both 1064 nm and 1120 nm were calculated using Equation 5 and the optical properties of each flight path. These gating times were chosen as the minimum amount of time it would take a photon to reach the blood layer, or where it would be in the case of the model without the blood. The only photons that were counted were photons whose time was greater than this threshold time. It is expected with great probability that photons will scatter and take a non-direct path through the tissue, but this value gives a reasonable minimum bound. The script showing these calculations can been seen in the Code Library in *gate_time_calculations.py*. The results are shown in the table below.

Table 9: Average Time of Flight with Gate

Wavelength	With Blood	Without Blood
1064 nm	1.748e-9	1.750e-9
1120 nm	1.730e-9	1.741e-9

Finally, the hypothesized pattern can be seen. By examining the average time of detected photons while using a gated detector, the model with the lower average time in both

1064 nm and 1120 nm is the model with the blood layer. This provides another viable method for differentiation between the two models, and thus potentially in the real world, too, as it is appropriately measurable. The differences in timing are now in the 10s of picosecond range. There exists more equipment capable of measuring with this precision, and thus it is more practical. One limitation of this gating method is its requirement of knowing the distances and properties of the tissues in the flight path of the photon. Given this information, however, it is a powerful tool for focusing on the relevant data, in addition to the implications gating has for real world detectors as mentioned in section 1.3. With reference to timing and measuring the average time of flight of photons, determining a difference between an area with and without blood is both possible and measurable by equipment commonly available on the market[a].

In addition to examining the measurable differences between models with and without a blood layer, there was also a desire to examine the ability of TD-DCS to differentiate between models with varying blood layer thicknesses. As a reminder, the default blood-layer size has been 5 mm in thickness. Below are the results of running the same test described for Table 8, but using more blood layer thicknesses.

Table 10: Average Time of Flight

Blood Thickness	1064 nm	1120 nm
2 mm	1.8057e-10	1.7940e-10
4 mm	1.8057e-10	1.7940e-10
6 mm	1.8056e-10	1.7940e-10
8 mm	1.8057e-10	1.7939e-10

As seen above, there is a similar issue as was seen in the results for Table 8. The photons being reflected at the dermis, as well as other early layers, are overwhelming the average and making any potential differences occurring within the liver and blood impossible

---

[a] https://www.picoquant.com/products/category/photon-counting-instrumentation

to measure. The hypothesized trend that would be ideally be seen in the results would be a steady decrease in average time as the blood thickness is increased. As there is a larger and larger highly reflective layer, the photons penetrating to this region would be more likely reflected; this would result in a quicker return time, and thus overall lower average time. While the trend cannot be seen in the ungated times, this trend can be seen in the results for the gated average time of flight, shown below.

Table 11: Average Time of Flight with Gate

Blood Thickness	1064 nm	1120 nm
2 mm	1.749796e-09	1.735384e-09
4 mm	1.749470e-09	1.735345e-09
6 mm	1.749128e-09	1.734529e-09
8 mm	1.748899e-09	1.734010e-09

Looking at the results shown above, there is a trend of average times shortening, but unfortunately these values are much less pronounced than the results shown in Table 9. At the picosecond resolution, the changes are just detectable. While if considering values smaller than a picosecond, then the trend can clearly be seen, it is important to limit the scope of timing resolution. This is motivated by the goal of having a handheld TD-DCS NCTH detection device. There are commercially available devices that have picosecond resolution, but even these are a bit large for the handheld world. Therefore, picosecond resolution is the limit of consideration. Under this limitation, there is a minimum thickness change required for differentiable results to be obtained in this model of four to six millimeters.
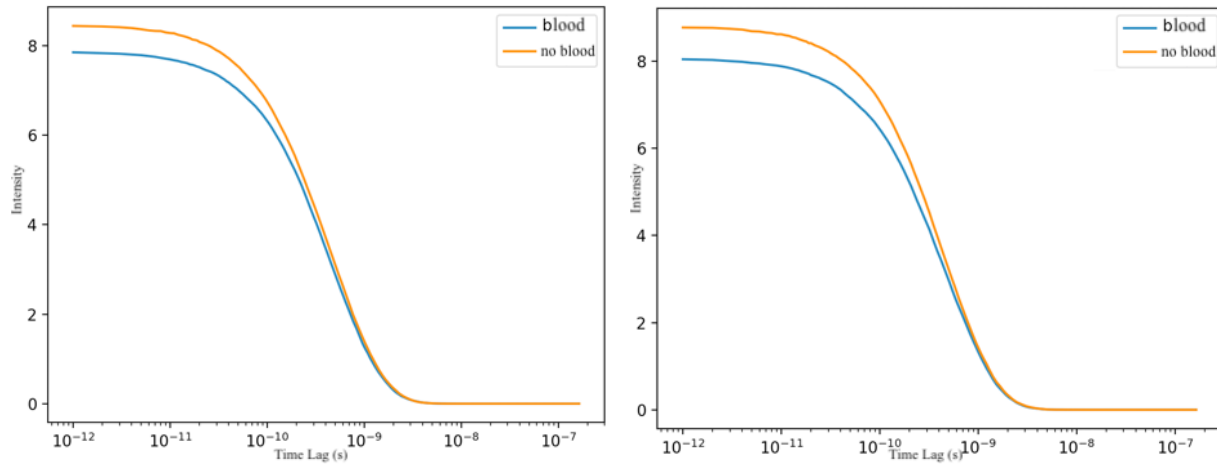
2.2.3 Autocorrelation

Section 1.5 alludes to the complicated process of using autocorrelations and biophysical relationships to determine flow from TD-DCS measurements. The ability to determine BFi from TD-DCS measurements is one of the biggest advantages to using this

imaging modality. As mentioned in section 1.5, one of the key components to the computation of this complex process is the measured intensity autocorrelation function. Using this measurement in tandem with the other equations provides enough information to determine blood flow. While this is typically the case, the considered models of this thesis are stationary, and do not have any flow. Therefore, in addition to these calculations being outside the scope of this thesis, the BFi potentially found would be meaningless. One portion of this process that is measurable and able to be calculated with the data from the model is the measured intensity autocorrelation. This section will discuss the process for the calculations as well as discussing their results and implications on how a real-world measurement would perform.

As found by the analysis in the previous section, there were identifiable differences between the models with and without blood for both 1064 nm and 1120 nm wavelength photons. In addition, capping the measurement data at picosecond resolution aligns closely with the real-world goals for a handheld device. With these considerations in mind, the intensity autocorrelation was computed for those four models with the timing resolution set to the picosecond range. These calculations were conducted for acquisition times of one and ten seconds, resulting in a generation of 80,000,000 and 800,000,000 photons respectively. Furthermore, in consideration of the results found in the previous section, all autocorrelations were taken using only gated data. Calculations were performed by *autocorrelation.py*.

Figure 5: Autocorrelations of 80,000,000 Photons

Figure 6: Autocorrelations of 80,000,000 Photons
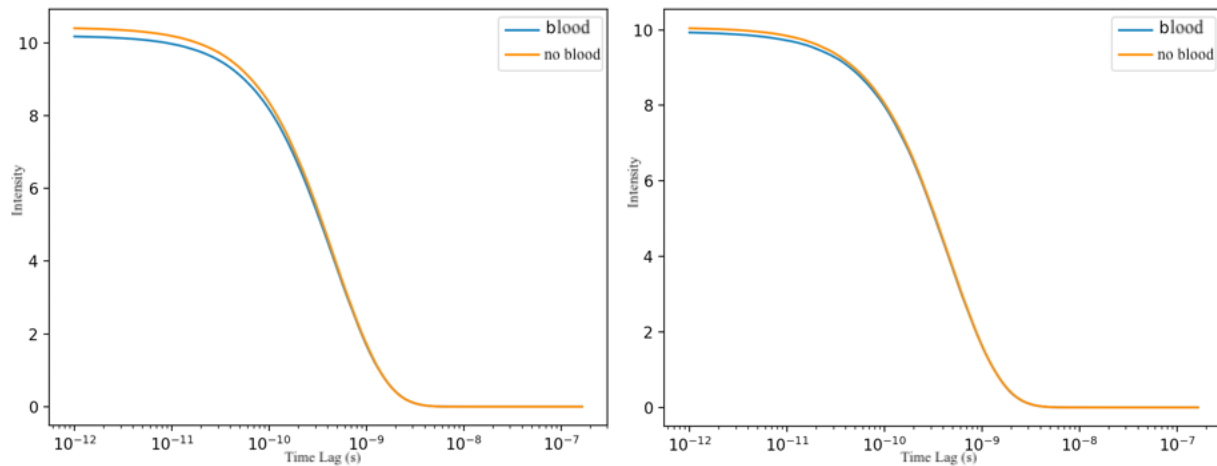
While normally the slope of the autocorrelation curve is proportionally to the flow, where a steeper slope would indicate more flow, these results cannot be interpreted using this metric due to the stationary model from which the analyzed data originates. However, these results can be used as another tool for differentiation. When comparing two models, one with the blood layer and one without, the autocorrelation curves are distinguishable. Given that both curves start and end their decay at the same location, and that the autocorrelations taken from the return signals for the models without a blood layer start at a greater magnitude, the autocorrelations from the models without blood layers have a

steeper average slope, giving a mathematical means for differentiation. While extrapolating BFi is impossible from this data set, the autocorrelation provides another analysis tool for differentiation between areas with and without blood. Most importantly, it shows that there are detectable differences in this medium and at this depth, therefore hinting that in potential future research detectable changes could be found in *in vivo* experiments as well.

2.2.4 Additional Real-World Analysis

The above sections provide example calculations of some of the analysis methods that are often used in TD-DCS measurements, but there are some computations that cannot be made from this model's data: flow values and blood oxygenation. While unable to make these calculations, this section will make the argument that there would be sufficient data if using TD-DCS on the torso in the real world and therefore would have sufficient information to perform the required calculations.

Section 2.2.3 examines autocorrelation curves as a means of differentiation between samples with and without blood, but as highlighted in section 1.5, the true purpose of the autocorrelation is an intermediate step to determining blood flow. With functioning code to compute autocorrelations already in place, to make an estimation of BFi, a future implementation would need only combine measurements from an *in vivo* sample and use the process mentioned in section 1.5 designed by Boas [10][11]. While this functionality could be created and applied to this data, it would not give any insight into blood flow as this model was static, but if TD-DCS measurements were taken using a real human, flow values could be determined.

TD-DCS can also allow for the determination of blood oxygenation. This process involves using two wavelengths to identify the concentration of both deoxy- and oxy-hemoglobin. Though usually made by diffuse optical spectroscopy (DOS), by comparing

relative values from two different wavelengths, this functionality could be incorporated into this hypothesized device [39]. Though the two wavelengths are on the same side of the isosbestic point near 800 nm that is often used, the values for oxygenated blood and deoxygenated blood are different enough at both 1064 nm and 1120 nm that they can be used with some modification to the original calculation methodology. While the usefulness of this information towards NCTH identification is yet untested, it shows the capability of this system to be used in a use-case where blood oxygenation is an important aspect to the results.

2.3 Measure of Success

The sections above expound upon the capabilities of TD-DCS, and show its capability to generate data that can be analyzed via many methods. While there is a lot of potentially compelling data, there still exists the determination of whether TD-DCS would provide enough information to be a truly viable method for NCTH detection. There are two main considerations for this determination: could TD-DCS potentially provide enough information for a diagnosis and how does it compare to existing methodologies, some of which were mentioned in section 1.6.

TD-DCS has been shown to have enough depth penetration at both 1064 nm and 1120 nm to reach the hepatic vein within the model and the simulated blood posterior to the vein. Being able to reach this region with enough consistency to get dependable returns provides plenty of data for calculating both average time of flight of photons and autocorrelations. The photon intensity autocorrelation provides sufficient information to compute a BFi value, and given a real subject or medium with flow, the calculated value would have meaning. Finally, because there was shown to be penetration for two different wavelengths, blood oxygenation could be extrapolated. TD-DCS, as modeled in this thesis, can detect differences between models with and without blood on a scale that is measurable not only by modeling, but on a

scale that real world instruments can measure. It is thus possible that TD-DCS could see the differences in a human as well and be useful for a NCTH diagnosis.

NCTH is an often-complicated injury, however. It can result in complex internal bleeding, with bleeding from multiple sources. Therefore, while TD-DCS potentially shows promise in the liver and for the hepatic vein, there is sufficient need for further research. If TD-DCS were to be considered as a method that could detect any bleed in the torso, then more testing, both in modeling and on real humans, would need to be pursued. The modeled measurements in this thesis had the benefit of ideal conditions with none of the complications that the real world often brings, such as hardware inconsistences, anatomical differences from person to person, and human operator error.

Modeling and early prototyping are essential in determining the viability of an idea and necessary for deciding whether to continue pursuing the idea. With respect to science alone, the results above indicate that there is a potential viability to NCTH detection via TD-DCS, and that there would be merit in further pursuing the imaging modality for this use-case. There is, however, another very important consideration: would TD-DCS improve existing methods enough that it would be relevant? There are existing imaging modalities that already identify internal bleeding, and while fMRI and CT scans have their shortcomings, such as being too large to be usable in the field and poorer temporal resolution, there are other methods that are now vying for the same space that TD-DCS is aiming to fill.

Over the past few years a new method called focused assessment with sonography for trauma (FAST) has been gaining in popularity and is now often used as a more portable measurement tool for NCTH and internal bleeding diagnoses [40][41]. FAST uses a handheld ultrasound device to search for free fluid in the torso. Fluid detection is the important caveat with FAST. Unlike TD-DCS, which has specificity to blood in its return signal, ultrasonic methods, like FAST, look for free fluid and assume that it is blood. There is a risk of false

positive results reflecting some tumors and other fluidic masses in the torso [41]. An additional shortcoming of FAST is the inherently limited spatial resolution of ultrasound. Even with these drawbacks, however, FAST is still quite powerful and a commonly used procedure in hospital emergency rooms [42].

While FAST may currently satisfy some medical professionals [43], there is room for improvement. NCTH is a lethal trauma injury, and when the safety and life of a human is in the balance, the medical field at large must seize upon every opportunity for the betterment of lifesaving tools, procedures, and technologies. TD-DCS has already shown extreme promise in its application within the brain [38], and more use-cases are certainly a possibility. There is potential, too, for TD-DCS as a tool for NCTH identification, and it would be worthwhile to confirm or disprove this with further test bench experiments. Section 3 will describe a potential path forward for future work.

3 Future Work

There are two clear opportunities for furthering the research of TD-DCS's ability for measurement inside the torso: test bench verification and *in vivo* testing. While the above results show promise for a TD-DCS system in making measurements within the torso, there is a requirement to conduct further experimentation beyond modeling before further conclusions can be drawn. Because there are already working TD-DCS systems for the brain, test bench and *in vivo* testing for the torso would only require modification of existing designs and could draw from already completed work [4].

Another avenue for future work, which could be used by TD-DCS applications regardless of the area of the body measurement occurs, mentioned in passing in section 2.2.2 was the limitation of the gating as a solution to being overwhelmed by large amounts of irrelevant data. In order to use gating to select for a specific layer of tissue, the target tissue

media must be well understood. In this model, the layers were precisely defined and it was known what the photons were interacting with, thus determining a gating time was possible. One important creation would be an algorithm that could automatically adjust its gating time to search for regions of interest within the return signal. This would allow an operator of a potential TD-DCS device to move from region to region without needed to completely recalibrate the device manually. Furthermore, even if the device was being used to measure one region only across multiple patients, each body is unique and thickness layers will vary. An algorithm that could adjust the timing of the photon gating by examining trends in the return pattern would be very powerful.

This thesis has shown that there is potential for the use of TD-DCS within the torso. While there is a lot of research for TD-DCS and its applications within the brain, TD-DCS has capabilities to extend to other areas of the body as well. While other competing technologies for NCTH identification and diagnosis are also expanding, these projects only highlight the welcome progress within the medical field. It is important to never limit the scope of research that can develop methodologies, equipment, and techniques for saving lives.

4 Code Library

CreateMCXConfig.m

```matlab
 1 %% Layer Thickness Vectors
 2 %layer = row vector of tissue thicknesses in mm (e.g. [1 1 3 5])
 3 air_buffer_layer  = 1;
 4 dermis_th         = 2;
 5 subcutaneousfat_th = 11;
 6 muscle_th         = 17;
 7 abdominalfat_th   = 16;
 8 liver_1_th        = 30;
 9 liver_hep_th      = 5;
10 liver_hep_bleed   = 2;
11 liver_2__th       = 30;
12 liver_vc_th       = 7;
13
14 layer_vector=[air_buffer_layer, air_buffer_layer, dermis_th,
15              subcutaneousfat_th, muscle_th, abdominalfat_th,
16              liver_1_th,liver_hep_th,liver_hep_bleed,liver_2__th,liver_vc_th];
17
18 %% Optical Property Vectors
19 % op_props = matrix of tissue types (rows) by four tissue values (col)
20 % [ua1, us1, g1, n1;
21 %   ua2, us2, g2, n2];
22 %          ua = tissue absorption mm-1
23 %          us = tissue scatter mm-1
24 %          g = tissue average cosine of scatter.
25 %          n = tissue index of refraction
26 air_buffer         = [0 0 1 1];
27 dermis_op          = [.008 8.5 .8 1.37];
28 subcutaneousfat_op = [.105 9.4 .91 1.44];
29 muscle_op          = [.15 12.5 .96 1.37];
30 abdominalfat_op    = [.22 4.4 .91 1.37];
31 liver_op           = [.045 36.3 .96 1.38];
32 blood              = [.47 63.9 .993 1.36];
33
34 op_vector=[air_buffer; air_buffer; dermis_op;
35         subcutaneousfat_op; muscle_op; abdominalfat_op;
36         liver_op; liver_op; blood; liver_op; liver_op];
37
38 %% Create Simulation File for MCX
39 for i=1:1000 %Generates 1000 Testing Files
40     ParameterFileSetup(layer_vector,op_vector,i,50,50)
41 end
```

mch_txt.m

```matlab
 1 n_values=[1, 1.38, 1.44, 1.37, 1.46, 1.38, 1.38, 1.363, 1.38, 1.38];
 2 data=loadmch(filename{1});
 3 total_photons=length(data);
 4 times=zeros(1,total_photons);
 5 for k=1:total_photons
 6     event=data(k,1:end);
 7     time_of_flight=0;
 8     for j=1:10
 9         time_of_flight=time_of_flight+event(j+2)/(1000*299792458/n_values(j));
10     end
11     times(k)=time_of_flight;
12 end
13 shuffled=times(randperm(length(times)));
14 mean=150e-12;
15 sigma=50e-12;
16 cdf_old=.5*(1+erf((0-mean)/(sigma*sqrt(2))));
17 number_to_release=0;
18 number_to_release_old=0;
19 delay_times=zeros(1,total_photons);
20 photon_old=0;
21 for c=0:299
22     c=c*1e-12;
23     cdf=.5*(1+erf((c-mean)/(sigma*sqrt(2))));
24     number_to_release=floor((cdf-cdf_old)*total_photons);
25     cdf_old=cdf;
26     for photon=number_to_release_old+1:number_to_release_old+number_to_release
27         delay_times(photon)=shuffled(photon)+c;
28     end
29     number_to_release_old=number_to_release_old+number_to_release;
30 end
31 for t=1:total_photons
32     if delay_times(t)==0
33         break
34     end
35 end
36 delay_times=sort(delay_times(1:t-1));
37 txtfile=strcat('../extracted_data_g/',sub,'.txt');
38 fileID=fopen(txtfile{1},'w');
39 fprintf(fileID,'%15.11e\n',delay_times);
40 fileID=fclose(fileID);
```

create_pdf.py

```python
1  import os
2  import json
3  import time
4  #first determine bin width ranges from 0 to 15ns
5  buckets={}
6  step=.5e-13
7  full=int(round(15e-9/step))
8  for x in xrange(full):
9      x*=step
10     x_next=x+step
11     x=round(x,15)
12     x_next=round(x_next,15)
13     buckets[(x,x_next)]=0
14
15 bucket_keys=sorted(buckets.keys(),key=lambda x: x[0])
16 text_files=os.listdir("../extracted_data_g/.")
17 visited=set()
18 count=1
19 while count<1000:
20     time.sleep(5)
21     print('Reloading All Data')
22     text_files=os.listdir("../extracted_data_g/.")
23     count=1
24     for file in text_files:#tqdm(text_files):
25         print(str(count)+'/'+str(len(text_files)))
26         count+=1
27         if file in visited:
28             print('Already Counted:',file)
29             continue
30         visited.add(file)
31         with open('./../extracted_data_g/'+file,'r') as txf:
32             last=0
33             for val in txf:
34                 time_=float(val)
35                 for i in xrange(last,len(bucket_keys)):
36                     bucket_key=bucket_keys[i]
37                     if time_>=bucket_key[0] and time_<bucket_key[1]:
38                         buckets[bucket_key]+=1
39                         last=i
40                         break
41 weights=[]
42 times=[]
43 t=0
44 total=sum(buckets.values())
45 for key in bucket_keys:
46     weights.append(buckets[key])
47     times.append(t)
48     t+=step
49
50 with open('./../pdf/weights.json','w') as js:
51     json.dump(weights,js)
52 with open('./../pdf/times.json','w') as js:
53     json.dump(times,js)
```

gating_time_calculations.py

```
1  def time_region(dist,n):
2      return dist*n/(1000*299792458)
3
4  #Index of refraction values
5  n_1064={'dermis':1.38,'sub_fat':1.44,
6          'muscle':1.37,'abd_fat':1.46,
7          'liver':1.38,'blood':1.363}
8  n_1120={'dermis':1.37,'sub_fat':1.44,
9          'muscle':1.37,'abd_fat':1.37,
10         'liver':1.38,'blood':1.36}
11
12 d_list=[2,11,17,16,30,5,5,30,7]
13 t_list=['dermis','sub_fat','muscle','abd_fat','liver','liver','blood','liver','liver']
14
15 estimated_time_to_blood_and_back_1064=0
16 estimated_time_to_blood_and_back_1120=0
17 for d,t in zip(d_list,t_list):
18     estimated_time_to_blood_and_back_1064+=(2*time_region((d),n_1064[t]))
19     estimated_time_to_blood_and_back_1120+=(2*time_region((d),n_1120[t]))
20 print(estimated_time_to_blood_and_back_1064)
21 print(estimated_time_to_blood_and_back_1120)
```

autocorrelation.py [44]

```
1  def autocorrelation(timestamps,max_lag_time,time_resolution):
2      #adapted from Danil 2016
3      maxLag = math.ceil(max_lag_time/time_resolution)
4      diffs=np.diff(timestamps)
5      auto={0:0}
6      len_d=len(diffs)
7      for i in tqdm(range(len_d)):
8          j=0
9          cumulative=0
10         while (i+j < len_d) and (cumulative+diffs[i+j] <= maxLag):
11             cumulative+=diffs[i+j]
12             if cumulative>0:
13                 if cumulative in auto:
14                     auto[cumulative]+=1
15                 else:
16                     auto[cumulative]=1
17             j+=1
18     accumulation=[auto[i]*(timestamps[-1]-timestamps[0])/(len(timestamps)**2) for i in sorted(auto.keys())]
19     t=[i*time_resolution for i in range(len(accumulation))]
20     return accumulation, t
```

sample.py [45]

```python
1  import json
2  import math
3  import random
4  import bisect
5
6  with open('./../pdf/weights.json','r') as js:
7      weights=json.load(js)
8  with open('./../pdf/times.json','r') as js:
9      times=json.load(js)
10
11 class WeightedRandomGenerator(object):
12     #https://eli.thegreenplace.net/2010/01/22/weighted-random-generation-in-python
13     def __init__(self, weights):
14         self.totals = []
15         running_total = 0
16         for w in weights:
17             running_total += w
18             self.totals.append(running_total)
19     def next(self):
20         rnd = random.random()*self.totals[-1]
21         return bisect.bisect_right(self.totals, rnd)
22     def __call__(self):
23         return self.next()
24
25 p=WeightedRandomGenerator(weights)
26
27 num_pulses=80e6
28 photons_per_pulse=1
29 timestamps=[]
30 for i in range(int(num_pulses)):
31     for j in range(int(photons_per_pulse)):
32         new_photon=times[p()]#generate photon
33         timestamps.append(round(new_photon+i/freq,14))#round to picoseconds
34
35 auto dict, t dict = autocorrelation(timestamps,1e5,1e-12)
```

References

[1] F. Scholkmann, S. Kleiser, A. J. Metz, R. Zimmermann, J. Mata Pavia, U. Wolf, and M. Wolf, "A review on continuous wave functional near-infrared spectroscopy and imaging instrumentation and methodology," NeuroImage, vol. 85, Jan. 2014. doi: 10.1016/j.neuroimage.2013.05.004.

[2] Scholkmann F, Wolf M. "General equation for the differential pathlength factor of the frontal head depending on wavelength and age." Journal of biomedical optics, vol. 18, no. 10, 2013. Accessed 9 Aug. 2018.

[3] Xiaojun Cheng, Davide Tamborini, Stefan A. Carp, Oleg Shatrovoy, Bernhard Zimmerman, Danil Tyulmankov, Andrew Siegel, Megan Blackwell, Maria Angela Franceschini, and David A. Boas, "Time domain diffuse correlation spectroscopy: modeling the effects of laser coherence length and instrument response function," Opt. Lett. 43, 2756-2759 (2018)

[4] Sutin, Jason et al. "Time-domain diffuse correlation spectroscopy." Optica vol. 3,9 (2016): 1006-1013. doi:10.1364/OPTICA.3.001006

[5] Osawa T., Shiose K., Takahashi H. (2017) Tissue Blood Volume Parameters Measured by Continuous-Wave and Spatially Resolved NIRS Show Different Changes During Prolonged Cycling Exercise. In: Halpern H., LaManna J., Harrison D., Epel B. (eds) Oxygen Transport to Tissue XXXIX. Advances in Experimental Medicine and Biology, vol 977. Springer, Cham

[6] Glover, Gary H. "Overview of functional magnetic resonance imaging." Neurosurgery clinics of North America vol. 22,2 (2011): 133-9, vii. doi:10.1016/j.nec.2010.11.001

[7] B. F. Aull, E. K. Duerr, J. P. Frechette, K. A. McIntosh, D. R. Schuette and R. D. Younger, "Large-Format Geiger-Mode Avalanche Photodiode Arrays and Readout Circuits," in IEEE Journal of Selected Topics in Quantum Electronics, vol. 24, no. 2, pp. 1-10, March-April 2018, Art no. 3800510.

[8] Vo-Dinh, Tuan. Biomedical Photonics Handbook: Therapeutics and Advanced Biophotonics. CRC Press Inc, 2014.

[9] "Autocorrelation." Wikipedia, Wikimedia Foundation, 10 Apr. 2019, en.wikipedia.org/wiki/Autocorrelation.

[10] D. A. Boas, L. E. Campbell, and A. G. Yodh, "Scattering and Imaging with diffusing temporal field correlations," *Phys. Rev. Lett.* (1995)

[11] D. A. Boas and A. G. Yodh, "Spatially varying dynamical properties of turbid media probed with diffusing temporal light correlation," *J. Opt. Soc. Am.* (1997).

[12] Kisat, Mehreen et al. "Epidemiology and outcomes of non-compressible torso hemorrhage" Journal of Surgical Research, Volume 184 , Issue 1 , 414 – 421

[13] Giannakopoulos, Triantafillos G, and Efthymios D Avgerinos. "Management of Peripheral and Truncal Venous Injuries." Frontiers in surgery vol. 4 46. 24 Aug. 2017, doi:10.3389/fsurg.2017.00046

[14] Morrison, JJ, et al. "Injury Pattern and Mortality of Noncompressible Torso Hemorrhage in UK Combat Casualties." Advances in Pediatrics., U.S. National Library of Medicine, Aug. 2013, www.ncbi.nlm.nih.gov/pubmed/23883918.

[15] Qianqian Fang and David Boas, "Monte Carlo Simulation of Photon Migration in 3D Turbid Media Accelerated by Graphics Processing Units," Opt. Express, vol. 17, issue 22, pp. 20178-20190 (2009).

[16] "Lincoln Laboratory Supercomputing Center." MIT Lincoln Laboratory, www.ll.mit.edu/r-d/cyber-security-and-information-sciences/lincoln-laboratory-supercomputing-center.

[17] Morrison, Jonathan & Rasmussen, Todd. (2012). Noncompressible Torso Hemorrhage A Review with Contemporary Definitions and Management Strategies. The Surgical clinics of North America. 92. 843-58, vii. 10.1016/j.suc.2012.05.002.

[18] American National Standard for Safe Use of Lasers. ser. Z136.1, Laser Institute of America, 2014.

[19] Selb, Juliette et al. "Sensitivity of near-infrared spectroscopy and diffuse correlation spectroscopy to brain hemodynamics: simulations and experimental findings during hypercapnia." Neurophotonics vol. 1,1 (2014): 015005. doi:10.1117/1.NPh.1.1.015005

[20] "Skin Anatomy and Physiology." Nu Skin, www.nuskin.com/en_ZA/corporate/company/science/skin_care_science/skin_anatomy_andphysiology.html.

[21] Akkus O, Oguz A, Uzunlulu M, Kizilgul M (2012) Evaluation of Skin and Subcutaneous Adipose Tissue Thickness for Optimal Insulin Injection. J Diabetes Metab 3:216. doi:10.4172/2155-6156.1000216

[22] Sugimoto, Takamune et al. "Changes in thickness of the transversus abdominis during the abdominal drawing-in manoeuvre and expiratory muscle training in elderly people." Journal of physical therapy science vol. 30,1 (2018): 119-123. doi:10.1589/jpts.30.119

[23] Kim, Jungmin et al. "Thickness of rectus abdominis muscle and abdominal subcutaneous fat tissue in adult women: correlation with age, pregnancy, laparotomy, and body mass index." Archives of plastic surgery vol. 39,5 (2012): 528-33. doi:10.5999/aps.2012.39.5.528

[24] Tong, Yubing et al. "Optimization of abdominal fat quantification on CT imaging through use of standardized anatomic space: a novel approach." Medical physics vol. 41,6 (2014): 063501. doi:10.1118/1.4876275

[25] Wolf DC. Evaluation of the Size, Shape, and Consistency of the Liver. In: Walker HK, Hall WD, Hurst JW, editors. Clinical Methods: The History, Physical, and Laboratory Examinations. 3rd edition. Boston: Butterworths; 1990. Chapter 94. Available from: https://www.ncbi.nlm.nih.gov/books/NBK421/

[26] Michael, Wells L., Michael, Fenstad,. Et al. "Imaging Findings of Congestive Hepatopathy." RadioGraphics, pubs.rsna.org/doi/10.1148/rg.2016150207?url_ver=Z39.88-2003&rfr_id=ori:rid:crossref.org&rfr_dat=cr_pub=pubmed.

[27] Salomatina, E., B. Jiang, J. Novak, and A. N. Yaroslavsky. 2006. Optical properties of normal and cancerous human skin in the visible and near-infrared spectral range. Journal of Biomedical Optics 11(6):9.

[28] van Gemert, M. J. C., J. S. Nelson, S. L. Jacques, H. J. C. M. Sterenborg, and W. M. Star. 1989. Skin optics. IEEE Transactions on Biomedical Engineering 36(12):1146–1154.

[29] Ding, H. F., J. Q. Lu, W. A. Wooden, P. J. Kragel, and X. H. Hu. 2006. Refractive indices of human skin tissues at eight wavelengths and estimated dispersion relations between 300 and 1600 nm. Physics in Medicine and Biology 51(6):1479–1489.

[30] Bashkatov, A. N., E. A. Genina, V. I. Kochubey, and V. V. Tuchin. 2005. Optical properties of human skin, subcutaneous and mucous tissues in the wavelength range from 400 to 2000 nm. Journal of Physics D-Applied Physics 38(15):2543–2555.

[31] Muller, G. and A. Roggan, eds. 1995. Laser-Induced Interstitial Thermotherapy. Vol. PM25. Bellingham, WA: SPIE Press.

[32] Yang, Ye & Soyemi, Olusola & Landry, Michelle & Soller, Babs. (2005). Infulence of a fat layer on the near infrared spectra of human muscle: Quantitative analysis based on two-layered Monte Carlo simulations and phantom experiments. Optics express. 13. 1570-9. 10.1364/OPEX.13.001570.

[33] Rami Nachabe, Benno H. W. Hendriks, Adrien E. Desjardins, Marjolein van der Voort, Martin B. van der Mark, Henricus J. C. M. Sterenborg, "Estimation of lipid and water concentrations in scattering media with diffuse optical spectroscopy from 900 to 1600 nm," J. Biomed. Opt. 15(3) 037015 (1 May 2010)

[34] Marchesini, R., A. Bertoni, S. Andreola et al. 1989. Extinction and absorption coefficients and scattering phase functions of human tissues in vitro. Applied Optics 28:2318–2324.

[35] Yaroslavsky, A. N., I. V. Yaroslavsky, T. Goldbach, and H. J. Schwarzmaier. 1996b. The optical properties of blood in the near infrared spectra range. Proceedings of the SPIE 2678.

[36] Cheng, S., H. Y. Shen, G. Zhang, C. H. Huang, and X. J. Huang. 2002. Measurement of the refractive index of biotissue at four laser wavelengths. Proceedings of the SPIE 4916.

[37] Kang, Yooli & X. Lu, H & Lo, Yu-Hwa & S. Bethune, D & Risk, W.P.. (2003). Dark count probability and quantum efficiency of avalanche photodiodes for single-photon detection. Applied Physics Letters. 83. 2955-2957. 10.1063/1.1616666.

[38] Tamborini, Davide. "Detectors Challenges for Diffuse Correlation Spectroscopy at 1064 Nm." Optics@Martinos at Photonics West 2019. http://optics.martinos.org/opticsmartinos-at-spie-photonics-west-2019/

[39] Chao Zhou, Regine Choe, Natasha S. Shah, Turgut Durduran, Guoqiang Yu, Amanda Durkin, David Hsiang, Rita Mehta, John A. Butler, Albert E. Cerussi, Bruce Jason Tromberg, Arjun G. Yodh, "Diffuse optical monitoring of blood flow and oxygenation in human breast cancer during early stages of neoadjuvant chemotherapy," J. Biomed. Opt. 12(5) 051903 (1 September 2007)

[40] "Focused assessment with sonography for trauma." Wikipedia, Wikimedia Foundation, 10 Apr. 2019, en.wikipedia.org/wiki/Focused_assessment_with_sonography_for_trauma.

[41] Savatmongkorngul, Sorravit et al. "Focused assessment with sonography for trauma: current perspectives." Open access emergency medicine: OAEM vol. 9 57-62. 26 Jul. 2017, doi:10.2147/OAEM.S120145

[42] Laine, Jonathan M.D. Personal Interview. December 2018.

[43] Colonel Davis. Personal Interview. November 2018.

[44] Tyulmankov, Danil. "Time-Domain Diffuse Correlation Spectroscopy: Instrument Prototype, Preliminary Measurements, and Theoretical Modeling." DSpace@MIT, Massachusetts Institute of Technology, 1 June 2016, dspace.mit.edu/handle/1721.1/113444.

[45] Bendersky, Eli. "Weighted Random Generation in Python." Eli Benderskys Website ATOM, eli.thegreenplace.net/2010/01/22/weighted-random-generation-in-python.